Deactivation dynamics of a Ni supported catalyst during the steam reforming of volatiles from waste polyethylene pyrolysis

Aitor Ochoa, Itsaso Barbarias, Maite Artetxe, Ana G. Gayubo, Martin Olazar, Javier Bilbao, Pedro Castaño*

Department of Chemical Engineering, University of the Basque Country (UPV/EHU), P.O. Box 644-48080, Bilbao, Spain

ARTICLE INFO

ABSTRACT

The valorization of waste high density polyethylene (HDPE) for hydrogen production has been studied in a two-step process, comprising pyrolysis and subsequent steam reforming of the volatiles produced in the first step. Particularly, this work focuses on the deterioration mechanisms (sintering and coke deposition) of the Ni commercial catalyst used in the second step, as it conditions the overall process performance. Pyrolysis of HDPE has been performed in a conical spouted bed reactor at 500 °C, and the catalytic steam reforming of the pyrolysis volatiles, in a fluidized bed reactor at 700 °C. Deactivated catalyst samples were recovered at different values of time on stream, and characterized using XRD, N_2 adsorption-desorption, SEM and TEM electronic microscopies, temperature programmed oxidation (TPO), Raman, FTIR and LDI-TOF MS spectroscopies. The results show that the deactivation is due to the sintering and encapsulation –by coke– of Ni. The former is inevitable within the current conditions, and the latter can be ascribed to the condensation of adsorbed precursors that evolve over time. Encapsulating coke is partially carbonized into filamentous coke with lower effect on catalytic deactivation and higher economic interest.

© 2017 Elsevier B.V. All rights reserved.

1. Introduction

Plastic wastes are a great source of chemicals and fuels due to the following facts: (1) their world production shows a continuous increasing trend, registering a global production of 311 million tons in 2014 [1], (2) the subsequent dumping, generating a serious environmental problem due to their low biodegradability [2], and (3) their favorable chemical composition. Europe reached a plastic waste generation of 25.8 million tons in 2014, from which 30.8% went to landfill and 69.2% was used for recycling or incineration [1]. Polyolefins involved approximately 49% of the plastic demand, consisting of high density polyethylene, low density polyethylene and linear low density polyethylene (HDPE, LDPE and LLDPE, respectively) and polypropylene (PP). The USA registered a municipal plastic waste generation of almost 32 million tons in 2012 (63% polyolefins), from which 8.8% was recovered [3]. Taking this all into account, the valorization of waste plastics, and polyolefins in particular, turns out to be essential, in order to counteract this increasing worldwide consumption and its effects in the environment within the sustainable development [4].

Tertiary recycling of waste plastics by means of pyrolysis is considered the most attractive strategy to valorize these residues on a large scale in the consumer society [5,6]. Consequently, the pyrolysis of plastics has received great attention and acquired notable technological development [7,8]. Furthermore, pyrolysis units are relatively simple, respectful with environment and may be placed next to the collection and classification points of urban solid waste. On the other hand, the composition of products can be modified by incorporating acid catalysts to the pyrolysis reactor [9].

The studies on thermal or catalytic pyrolysis of waste polyolefins have been mainly targeting the monomer recovery [10–13] or the production of diesel fuel [14–16]. Pyrolysis of polyolefins at low temperature (500 °C) allows the selective production of pyrolysis waxes (C_{21+}) which can be fed into refinery units such as the catalytic cracker or the catalytic reformer, alone or together with the regular feed [17–19]. Besides, intending the production of monomers, the volatiles of the pyrolysis can be further treated with an in-line second step, such as secondary thermal cracking [20] or catalytic cracking [21–24]. The advantages of the sequenced two-step process are: (i) higher versatility when operating at the

optimum temperature in each step; (ii) lower catalyst deactivation in the second transformation, without the problems inherent to the plastic melting on the catalyst. These advantages of the sequenced two-step process are attractive for H_2 production, by means of in-line catalytic reforming of the volatiles exiting from the pyrolysis reactor. In a pioneer work with this strategy, Czernik and French [25] studied the continuous and sequenced polypropylene pyrolysis and volatile reforming, in separated fluidized beds, yielding 80% H_2 (with respect to the theoretical maximum) using a naphtha reforming commercial catalyst in the second reactor. Wu and Williams [26–31] and Acomb et al. [32] studied the performance of different reforming catalysts and conditions in this kind of sequenced pyrolysis-reforming of polyolefins. Furthermore, several authors [33,34] have employed fixed bed reactors in both steps. Erkiaga et al. [35], operating in continuous regime, proved the advantages of the conical spouted bed reactor (CSBR) in the first step of HDPE pyrolysis, due to the fact that the vigorous cyclic movement of sand particles covered by plastic avoids the bed defluidization. Moreover, the fast rate of mass and heat transport between phases allows obtaining a homogeneous volatiles stream consisting of C_{5+} hydrocarbons at low temperature (500 °C). These authors emphasize the limitation of the process due to the deposition of carbonaceous material (coke) in the reforming fixed-bed catalytic reactor. Barbarias et al. [36] have improved the system performance, using a fluidized bed reactor in the catalytic reforming step.

It is well stablished in the literature that deactivation of Ni catalysts in reforming reactions takes place due to coke deposition and Ni sintering. Several authors studied the evolution of coke content and nature in the reforming of hydrocarbons, such as methane [37,38] and propane [39], identifying two coke types: (i) Ni-encapsulating amorphous coke; and (ii) structured filamentous coke. The latter is sometimes called fibrillar or whisker-like coke and if the conditions are appropriate, it can be classified as carbon nanotubes (CNTs). Latorre et al. [40–42] proposed a mechanism of CNTs formation in which methane forms a metastable carbide, which releases carbon atoms that are diffused through the interphase of metallic nanoparticles, forming the nanotube after a nucleation stage. In the reforming of oxygenates, such as ethanol [43–46], dimethyl ether [47,48], and bio-oil [49], two main coke types were determined as well. In these works, the condensation of oxygenated reaction intermediates plays a major role in the rapid formation of amorphous and encapsulating coke, while the formation of structured coke is mainly due to CH_4 dehydrogenation and Boudouard reaction. All these works highlight the relevance of the feed composition and reaction conditions (temperature and steam/carbon ratio) on the content and nature of the deposited coke. These types of coke have been detected in the spent catalyst used in the production of hydrogen from polyolefins too [27,29–32]. On the other hand, it is well stablished that sintering is a noticeable deactivation cause in Ni catalysts, above temperatures in the range of 600–700 °C, depending on the catalyst structure, the operating conditions and the reaction medium composition [49–53].

This work focuses on the mechanisms of catalyst deactivation used in the second step of the sequenced pyrolysis-reforming of HDPE for hydrogen production. For this aim, we have used the same system used by Barbarias et al. [36] analyzing the evolution of catalyst and coke morphology at different stages of deactivation (values of time on stream). The dynamics of catalytic deactivation has been studied by means of X-ray diffraction (XRD), N_2 adsorption-desorption, scanning and transmission electron microscopies (SEM and TEM, respectively), temperature programmed oxidation (TPO), Raman spectroscopy, Fourier transformed infra-red (FTIR) spectroscopy and laser desorption/ionization time-of-flight mass spectrometry (LDI-TOF MS). The optimized operational conditions

Table 1
Mass composition (wt%) of volatiles from HDPE pyrolysis.

Fraction	Compound	Yield (wt%)	Fraction	Compound	Yield (wt%)
C_1–C_4		1.50	C_{12}–C_{20}		25.64
	Methane	0.03		Diolefins	3.22
	Ethane	0.06		Olefins	13.07
	Ethylene	0.08		Paraffins	9.35
	Propane	0.08	Waxes		67.00
	Propylene	0.50		Light (C_{21}–C_{40})	29.50
	Butanes	0.18		Heavy (C_{41+})	37.50
	Butenes	0.57			
C_5–C_{11}		5.86			
	Paraffins	0.34			
	Isoparaffins	2.50			
	Aromatics	0.28			
	Naftenes	0.19			
	Olefins	2.56			

for minimizing the impact of catalyst deactivation are suggested, together with a simplified mechanism of catalyst deactivation.

2. Experimental

2.1. Materials

The HDPE was provided by Dow Chemical (Tarragona, Spain) in the form of chipping (4 mm). The main properties are: average molecular weight, 46.2 kg mol^{-1}; polydispersity, 2.89; and density, 940 kg m^{-3}. The higher heating value, 43 MJ kg^{-1}, was determined by differential scanning calorimetry (Setaram TG-DSC-111) and isoperibolic bomb calorimetry (Parr 1356).

The reforming catalyst was provided by Süd Chemie (G90LDP catalyst) and its chemical formulation is based on NiO, CaAl$_2$O$_3$ and Al$_2$O$_3$. The catalyst has the form of perforated rings (19 × 16 mm) with a metallic phase of Ni supported on Al$_2$O$_3$, which is doped with Ca, with the NiO content being 14 wt%. This catalyst was ground and sieved to 0.4–0.8 mm, which is the suitable particle size to attain stable fluidization regime.

2.2. Operating conditions and composition of the reformed stream

Pyrolysis and in line steam reforming runs were carried out by continuously feeding HDPE in a bench scale plant, provided with a CSBR for the pyrolysis step and a fluidized bed reactor for the reforming step arranged in-line. A detailed description of the equipment has been previously reported elsewhere [36].

The operating conditions in the HPDE pyrolysis step are: 500 °C; HDPE inlet flow, 0.75 g min^{-1}; water flow, 3 ml min^{-1}; mass of silica sand, 50 g; sand particle diameter, 0.3–0.35 mm range. The steam reforming step of pyrolysis volatiles was carried out at the following operating conditions: 700 °C; space time, 16.7 g$_{catalyst}$ min g$_{HDPE}$$^{-1}$; steam/plastic mass ratio, 4 (steam/carbon molar ratio, 3.1). Table 1 displays the composition of the volatiles stream exiting the HDPE pyrolysis step, fed into the steam reforming step. It is noteworthy that the CSBR reaches complete conversion of HDPE into volatiles at 500 °C. The volatiles stream is mainly comprised of heavy waxes (C_{41+}, 37.5 wt%) and light waxes (C_{21}–C_{40}, 29.5 wt%), with a concentration of the fractions C_{12}–C_{20}, C_5–C_{11} and C_1–C_4 of 25.6, 5.9 and 1.5 wt%, respectively.

2.3. Characterization of fresh and used catalyst

The deactivation study was performed with runs at different time on stream values up to 185 min, with the aim of analyzing the catalyst in different deactivation degrees. The fluidized bed system

in this work and thus a uniform catalyst activity guarantees the representativeness of the analyzed catalyst.

Catalyst characterization was performed by means of several techniques: (i) the evolution of catalyst crystallographic structure and Ni^0 particle size was analyzed by XRD; (ii) the evolution of surface properties and both catalyst and coke morphology was studied by N_2 adsorption-desorption and SEM and TEM electronic microscopy; (iii) the evolution of coke content, structure and composition was studied by temperature programmed oxidation (TPO), Raman and FTIR spectroscopy and LDI-TOF MS analysis.

XRD analysis was performed in a Philips X'PERT PRO diffractometer, operating at 40 kV and 40 mA, in theta-theta configuration, with a secondary monochromator with $CuK\alpha_1$ radiation, at a wavenumber of 1.5418 Å. An energy dispersive PIXcel detector was used with an active length of $2\theta = 3.347$ Å. The average Ni^0 particle size was determined by applying the Debye-Scherrer approach at $2\theta = 52°$, corresponding to Ni^0 (200) plane.

The surface area, pore volume, and average pore size of the catalyst were measured by N_2 adsorption-desorption in a Micromeritics ASAP 2010 system by means of the conventional Brunauer-Emmett-Teller (BET) method. Experimental procedure consists on a degasification step at 150 °C during 8 h, followed by N_2 (99.9995%) adsorption-desorption.

SEM images were obtained in a JEOL JSM-7000F microscope with a tungsten filament (resolution 3.5 nm) equipped with an Oxford Pentafet energy-dispersive X-ray spectroscopic (EDX) analyzer (resolution 133 eV), operating at 20 kV, under vacuum at $9.65 \cdot 10^{-5}$ bar and intensity of $1.85 \cdot 10^{-10}$ A.

TEM images were obtained in a Philips SuperTwin CM200 microscope equipped with a LaB_6 filament and EDAX EDX microanalysis system, operating at 200 kV. Samples for the analysis were prepared via dispersion in ethanol solvent and deposition of a suspension drop on a carbon-coated copper grid (300 Mesh) followed by drying under vacuum.

TPO analysis was carried out in a Thermo Scientific TGA Q5000TA IR system, coupled on line with a Balzer Instruments Thermostar mass spectrometer in order to follow the evolution of combustion gases (mainly CO_2). Ground sample (5 mg) was first degasified with an inert 10 ml min^{-1} stream (N_2) for 5 min, and subsequently a 50 ml min^{-1} air stream was introduced, from 100 °C to 800 °C with a heating rate of 5 °C min^{-1}. The coke content was quantified from the CO_2 signal in the mass spectrometer during combustion, instead of the thermogravimetric signal, because Ni oxidation masks the latter signal.

Raman spectroscopic analysis were performed in a Reninshaw InVia confocal microscope using an excitation wavelength of 514 nm, performing the analysis in several areas of the sample for increased reproducibility.

FTIR spectroscopy was carried out in a FTIR Nicolet 6700 spectrometer, in transmission mode. Prior to the analysis of the deactivated sample, in order to subtract the influence of the catalyst on the IR spectrum, a sample is pelletized and analyzed, consisting of fresh catalyst (3–5 mg) on a KBr support (150 mg, purity above 99%), prepared by applying a pressure of 10 t cm^{-2} for 15 min. Subsequently, a pellet sample consisting of 3–5 mg of deactivated catalyst on a 150 mg of KBr support was prepared and analyzed after subtraction of the former sample signal.

LDI-TOF MS measurements were performed on a Bruker Autoflex Speed instrument (Bruker, Germany) equipped with a 355 nm Nd:YAG laser. All spectra were acquired in the positive-ion reflectron mode (accelerating voltage 20 kV, pressure 5×10^{-6} mbar). The sample (0.5 μl) was dissolved in THF at 10 g L^{-1}, prepared according to the "dry droplet" method.
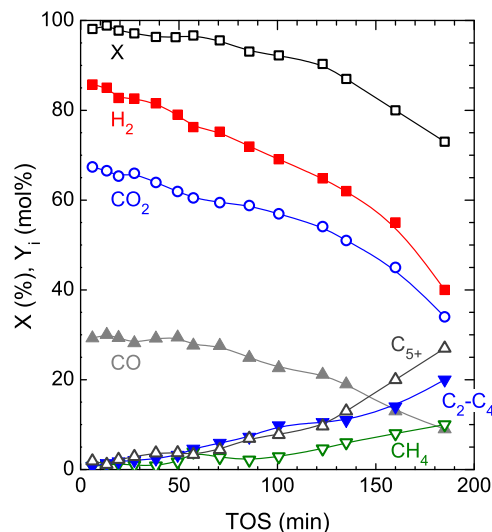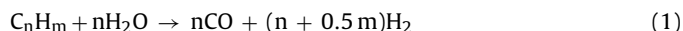

Fig. 1. Evolution with time on stream of the conversion of volatiles from HDPE pyrolysis (X) and yield of products (Y_i).

3. Results

3.1. Evolution with time on stream of reaction indices

Catalyst deactivation leads to a decrease in the rates of reactions involved in the reforming process: (1) hydrocarbon steam reforming and (2) water gas shift (WGS):

$$C_nH_m + nH_2O \rightarrow nCO + (n + 0.5\,m)H_2 \tag{1}$$

$$CO + H_2O \leftrightarrow CO_2 + H_2 \tag{2}$$

In order to quantify the deactivation, the following reaction indices were established, corresponding to the reforming step: conversion (X), yield of each i product (Y_i) and hydrogen yield (Y_{H_2})

$$X = \frac{\text{Carbon units in the gas stream}}{\text{Carbon units in the HDPE feed}} 100 \tag{3}$$

$$Y_i = \frac{\text{Carbon units in the } i \text{ product}}{\text{Carbon units in the HDPE feed}} 100 \tag{4}$$

$$Y_{H_2} = \frac{F_{H_2}}{F^0_{H_2}} 100 \tag{5}$$

where F_{H_2} and $F^0_{H_2}$ are the molar flows of hydrogen in the product stream and the maximum stoichiometric one, respectively. The stoichiometry corresponds to:

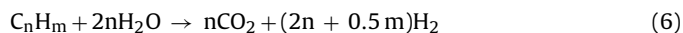$$C_nH_m + 2nH_2O \rightarrow nCO_2 + (2n + 0.5\,m)H_2 \tag{6}$$

Fig. 1 shows the effect of catalyst deactivation in the evolution of reaction indices with time on stream. H_2 and CO yields decrease in a similar trend to that of conversion, due to the fact that deactivation disfavors steam reforming reaction (Eq. (1)), as well as WGS reaction (Eq. (2)), resulting in a decrease in CO_2 yield. Consequently, yields of CH_4, C_2–C_4 and C_{5+} hydrocarbons are increased. It is worth noting that the decrease in the reaction indices is approximately linear up to 100 min of time on stream and subsequently decreases more sharply, coinciding with a notable increase in the concentration of hydrocarbons in the product stream. This change in the trend of the deactivation rate is later studied. In other words, the deactivation can be attributed to two pathways with a change in the dominant one at 100 min.
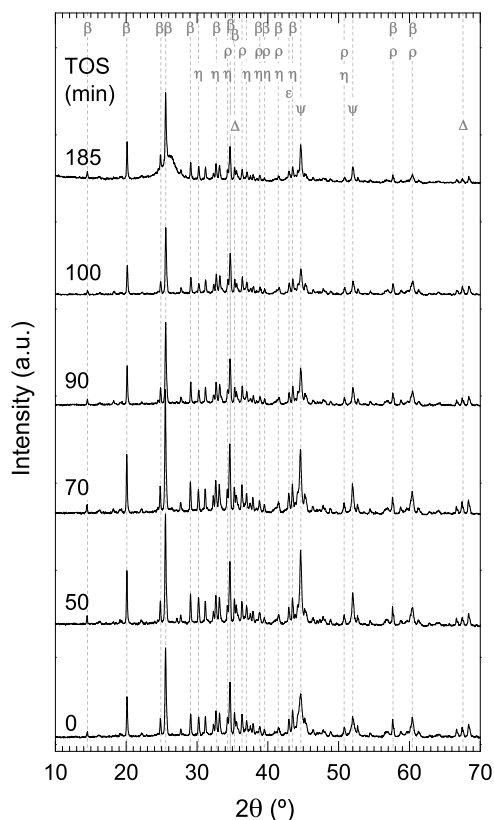
Fig. 2. XRD spectra of the reduced fresh catalyst (0 min) and deactivated at several values of time on stream. Assigned bands: Ni^0 (Ψ); NiO (ε); Al_2O_3 (Δ); $CaO(Al_2O_3)_2$ (β), $CaAl_2O_4$ (η); $CaAl_{12}O_{19}$ (ρ).

3.2. Ni phase dynamics

Fig. 2 shows the XRD diffractograms corresponding to reduced fresh catalyst and deactivated ones at several values of time on stream. The diffractograms show the assignment of several peaks at different diffraction angles (2θ) to a total of six crystalline phases, expressed as Greek symbols at the top of Fig. 2. The assignment was carried out as follows [53–55]: Ni^0, 44.7° in (111) plane and 52° in (200) plane; NiO, 43°; Al_2O_3, 35.4° and 67.3°; $CaO(Al_2O_3)_2$, 14.4°, 20°, 24.6°, 25.6°, 32.8°, 34.5°, 35.4°, 37.7°, 39.4°, 41.4°, 43.3°, 57.4° and 60.3°; $CaAl_2O_4$, 30.1°, 32.8°, 34.2°, 36.9°, 37.7°, 39.4°, 41.4°, 43.3° and 50.6°; $CaAl_{12}O_{19}$, 34.2°, 36.2°, 37.7°, 39.4°, 41.4°, 50.6°, 57.4° and 60.3°. This assignment leads to an overlapping of several phases in the same 2θ positions. Interestingly, at 185 min Fig. 2 shows a broad peak at ca. 26°, which overlaps with $CaO(Al_2O_3)_2$ (24.6° and 25.6°). This broad peak is commonly assigned to crystalline graphite [56], which implies that a highly graphitic and structured coke is deposited on the catalyst at 185 min. XRD spectra indicate the presence of Ni^0 crystalline phases which conserve their reduced state during the reaction, indicated by the low intensity of the NiO peak at $2\theta = 43°$. This is due to the reducing capacity of H_2 and CO_2 in the reaction medium, as well as the capacity of the formed coke to maintain Ni in its reduced phase, even when the catalyst is extracted to the oxidant atmosphere [57]. Besides, a broad band at ca. 26° indicate the presence of (002) graphitic planes corresponding to the deposited coke. The presence of this band and the absence of (hk0) and (hkl) indices indicate that the perceptible coke by XRD consists of turbostratic stacking of small graphitic layers without regularity in the direction perpendicular to those layers.

Ni^0 crystal size was calculated considering the Debye-Scherrer approach at $2\theta = 52°$, corresponding to Ni^0 (200) plane, whose evo-
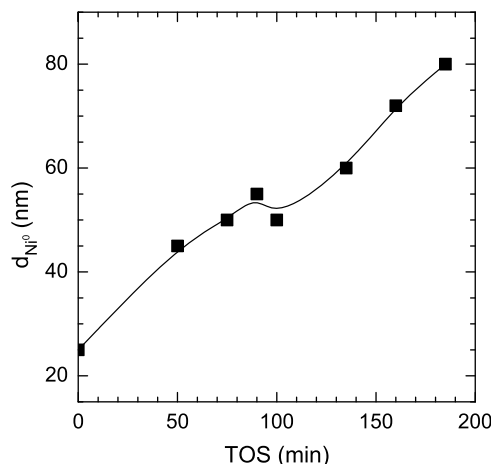

Fig. 3. Evolution with time on steam of Ni^0 crystal size of the catalyst, determined by XRD.

Table 2
Evolution with time on stream of the surface physical properties of the catalyst.

TOS (min)	S_{BET} ($m^2\,g^{-1}$)	V_{pore} ($cm^3\,g^{-1}$)	d_{pore} (Å)
0	19.0	0.111	122
50	8.7	0.072	362
75	8.3	0.074	362
90	8.9	0.072	338
100	8.0	0.070	372
135	8.0	0.062	384
185	64.0	0.247	152

lution is shown in Fig. 3. An increasing trend is observed in the size with time on stream, from 25 nm in the reduced fresh catalyst, to 80 nm at 185 min. These results evidence that Ni is sintering at 700 °C [58]. Interestingly, the evolution of Ni^0 crystal size can be ascribed to two zero-order (linear) rates of sintering: the first one between 0 and 100 min, and a second one from 100 min on. This behavior matches the observed deactivation shown in Fig. 1.

3.3. Catalyst morphology dynamics

Table 2 depicts the evolution with time on stream of the surface and structural properties of the catalyst, namely, surface area (S_{BET}), pore volume (V_{pore}) and average pore size (d_{pore}), determined from N_2 adsorption-desorption isothermal curves. Results show a sharp change of the catalyst porous structure at 50 min of time on stream, with a decrease in surface area from $19\,m^2\,g^{-1}$ in the reduced fresh catalyst, to $8.7\,m^2\,g^{-1}$. At the same time, total pore volume is decreased from $0.111\,cm^3\,g^{-1}$ to $0.072\,cm^3\,g^{-1}$ and the average pore size is increased from 122 Å to 384 Å in the deactivated catalyst. The catalyst properties slowly evolve with the same trend up to 135 min of time on stream, but a drastic change in the porous structure takes place at 185 min in the opposite direction. Hence, surface area at 185 min of time on stream is notably higher, $64.0\,m^2\,g^{-1}$. Total pore volume is also increased up to $0.247\,cm^3\,g^{-1}$, whereas average pore size is decreased down to 152 Å.

The observed evolution of the surface properties is a consequence of the growth of coke on catalyst. The initial blocking of micropores in the catalyst is related with the formation of encapsulating coke (0–50 min), whereas from a certain value of time on stream (185 min) coke contains filamentous structures that contribute to increase the surface area and pore volume. In the intermediate range (50–135 min), the contributions of both types of coke (encapsulating, leading to a decrease of surface area; and filamentous, leading the opposite behavior) are responsible of the steady value of surface area observed (8.0–8.7 $m^2\,g^{-1}$).
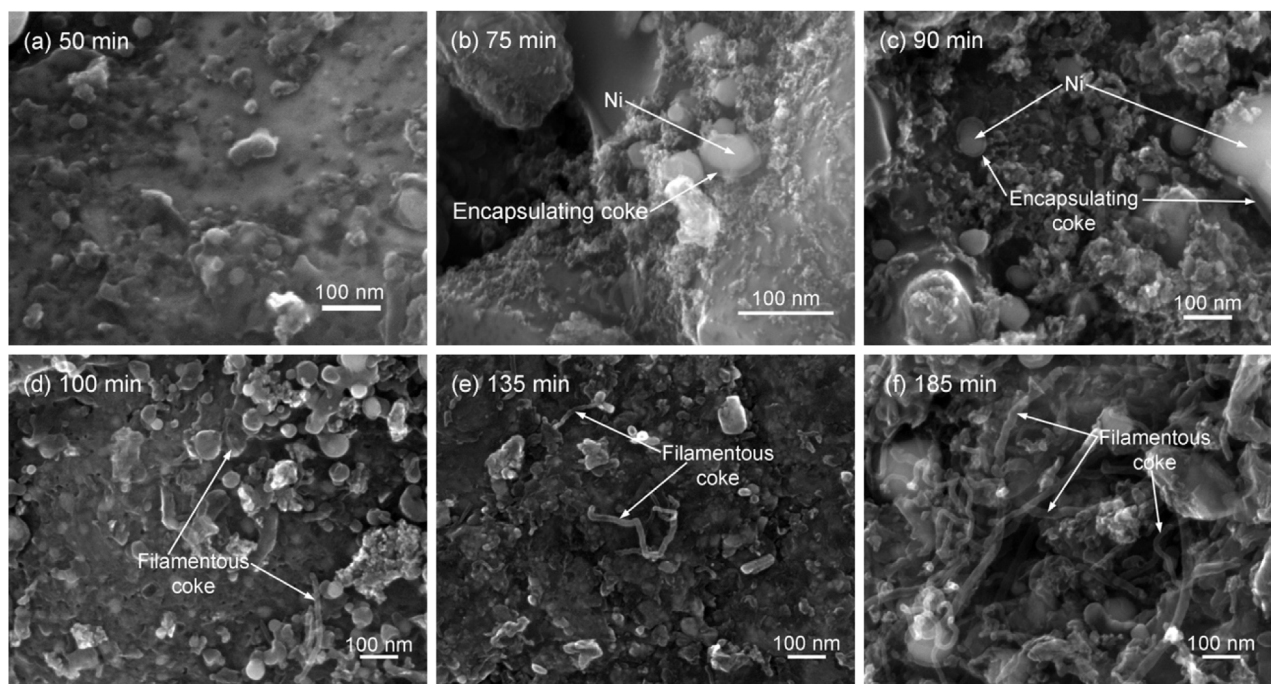
Fig. 4. SEM images of the catalyst used at several values of time on stream: 50 min (a); 75 min (b); 90 min (c); 100 min (d); 135 min (e); 185 min (f).

SEM images displayed in Fig. 4 reveal that up to 100 min (Fig. 4a–c) coke is deposited on the catalyst surface encapsulating the Ni particles. Subsequently, from 100 min on (Fig. 4d–f), filamentous coke is observed on the surface. This filamentous coke increases both in content and size with time on stream, resulting in a surface highly covered by filamentous coke at 185 min (Fig. 4f). These filaments are responsible of the increase in the surface area displayed at 185 min in Table 2.

Fig. 5 displays TEM images corresponding to the reduced fresh catalyst (Fig. 5a) and deactivated at three representative values of time on stream (Fig. 5b–g). For each deactivated catalyst images at two scales are shown. Ni^0 particles are identified in the images as the round-shaped darkest regions. Fig. 6 shows the distribution of the particle size measured from a representative number of TEM images, corresponding to the fresh and deactivated catalysts (100, 135 and 185 min). The distribution of Ni^0 particles becomes higher and broader upon the increase of time on stream, i.e. the sintering of Ni^0 leads to a bigger and more diverse particle sizes. The statistical parameters of the distribution curves shown Fig. 6 are summarized in Table 3. The average Ni^0 crystallite size values are similar to those determined from XRD patterns (Fig. 3), whereas the increasing standard deviation quantifies the size broadening with time on stream depicted in Fig. 6. The TEM images also reveal an evolution of the coke nature. Up to a time on stream of 100 min, coke is mainly present encapsulating the Ni particles. At 100 min of time on stream (Fig. 5b) both encapsulating coke and a nascent fraction of filamentous coke are observed. Subsequently, from 100 min on (Fig. 5b–g), an increasing fraction of filamentous coke is observed. These filaments also grow in length and diameter with time on stream, in the form of multi-walled filaments. Table 3 shows the evolution with time on stream of the size of filamentous coke, in terms of diameter and wall width. The results show a sequential increase in both the diameter and wall width of the deposited coke filaments, along with a sharp increase in the heterogeneity of their size, as suggested by the increase in the standard deviation values up to 185 min. This increased heterogeneity in both diameter and wall width of filaments at 185 min is well observed in Fig. 5g and f. Several authors obtained coke filaments of a diameter (ca.

15–20 nm) and wall thickness (ca. 5 nm) similar to those obtained at 100 and 135 min in the present work, during a two-stage pyrolysis of polymers and subsequent catalytic reforming/gasification of volatiles using Ni catalysts for H_2 production [30,59]. On the other hand, the zones with a lower contrast and definition in TEM images in Fig. 5 were ascribed as lower crystallinity phases corresponding to encapsulating coke, as well as Ca and Al oxides in the catalyst, though the assignment of the different phases are hardly distinguishable in the images.

Interestingly, Ni particles were not observed on the tip of the carbon nanotubes in the SEM or TEM images of this work. Multiple studies have proposed a mechanism of filamentous or nanotubular coke growth based on the fact that adsorbed carbon (in the form of Ni carbide) is diffused through the metallic particle, with a subsequent nucleation and precipitation on the base of that metallic particle. This continuous process separates physically the metallic particle from the surface on which it is supported, dragging it as the carbon filament grows, with a metallic particle on its tip [60–65]. This mechanism is dominant in the gas-phase carbonization of CO and CH_4, and the divergence of the present results is an indication that additional carbonization from adsorbed species is taking place, being these adsorbed species the so-called encapsulating coke. At the same time, this encapsulating coke is strongly influenced by the heterogeneity in the composition of HDPE pyrolysis products (feedstock of the reforming reactor), as well as by the different operating conditions. Moreover, metal-support interaction in the catalyst may be influential on the structure of the deposited coke, as well as on the location or size of surface Ni particles [66]. Therefore, although an increasing trend is observed in Table 3 with time on stream for both Ni^0 particle size and size of filamentous coke, it is not clear whether a direct relationship exists between the growth of the coke filaments and the Ni^0 particle size [30].

The group of Williams has envisioned applications of the filamentous coke deposited under analogous two-step processes from wastes like LDPE [32,67,68] or tires [59]. These applications are based on the fact that this filamentous coke resembles CNTs. However, the results obtained so far regarding the composition of filamentous coke indicate the relatively poor stacking order of the
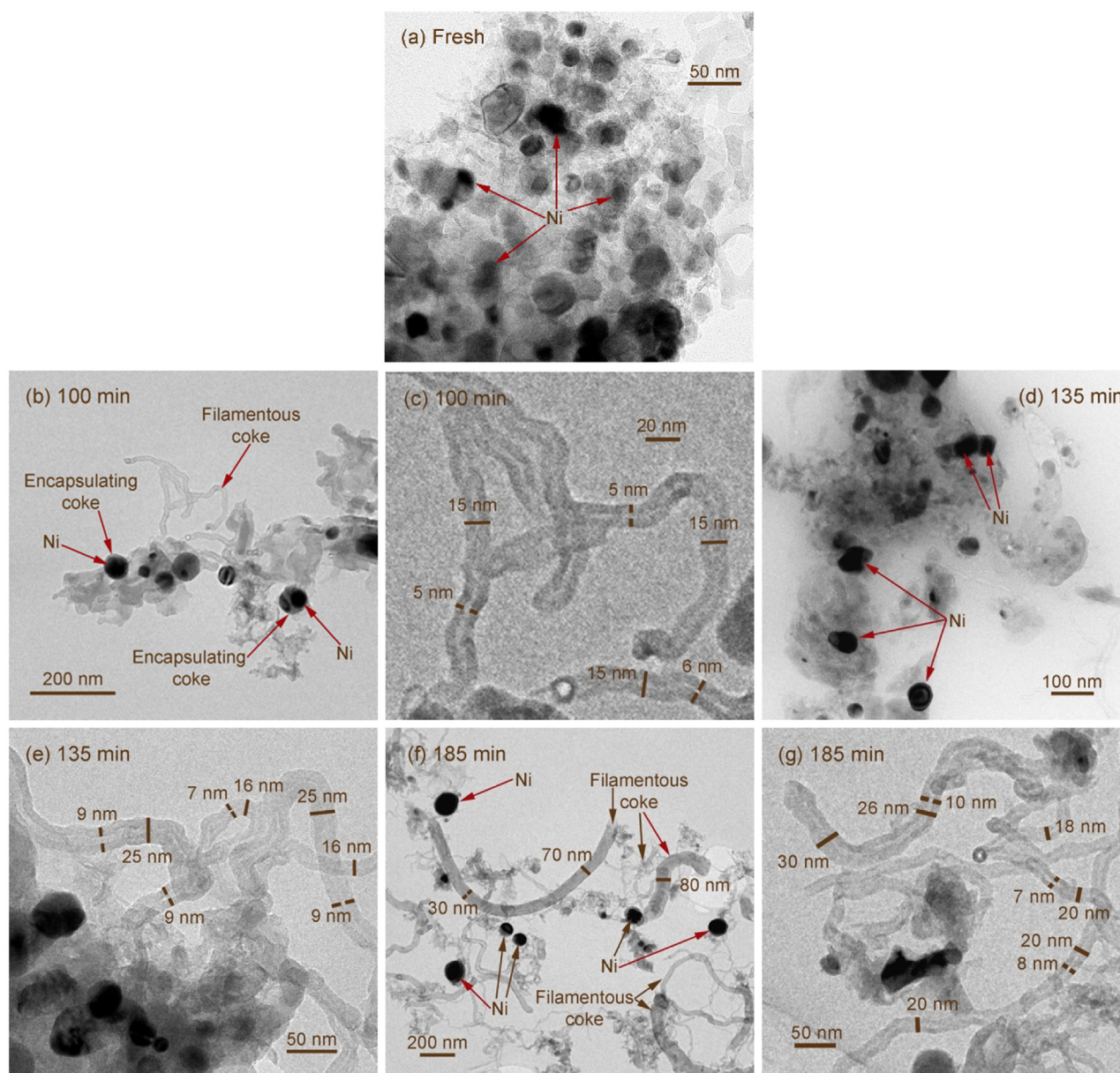
Fig. 5. TEM images of the fresh catalyst (a) and the used catalyst at several time on stream values: 100 min (b, c); 135 min (d, e); 185 min (f, g).

Table 3
Evolution with time on stream of the distribution of Ni crystal size, diameter and wall width of deposited filamentous coke, determined from TEM images.

TOS (min)	d_{Ni}^0 (nm)		Filamentous coke diameter (nm)		Filamentous coke wall width (nm)	
	Average	Standard deviation	Average	Standard deviation	Average	Standard deviation
0	24	5.0	–	–	–	–
100	49	10	15	1.8	5.3	0.6
135	61	20	19	2.7	7.1	0.8
185	83	24	27	15	11	6.8

filaments obtained in this work, so that for obtaining all the features of CNTs, it would be required and additional carbonization and graphitization of the already produced filaments.

3.4. Coke deposition dynamics

Fig. 7 shows the TPO profiles of the used catalysts at different values of time on stream. Results show two major temperature regions in which combustion takes place, indicating two different natures of coke. The first region shows a peak with a maximum at ca. 420–450 °C, whereas the second region displays a peak with a maximum at 510–580 °C. Furthermore, an increasing relative importance of this second peak is observed when increasing the time on stream. The existence of two peaks in the TPO analysis has been proved in literature, for Ni catalysts employed in steam reforming of CH_4 [62,69,70], volatiles of PP pyrolysis [27,30,71] and oxygenates [43–45,52,72–77]. Generally, the combustion peak at low temperatures (<500 °C in Fig. 7), is ascribed to coke hav-
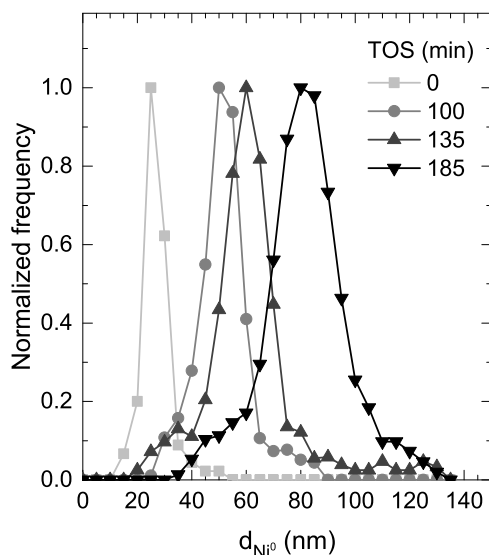
Fig. 6. Evolution with time on stream of the distribution of Ni^0 crystal size of the catalyst, based on TEM images.

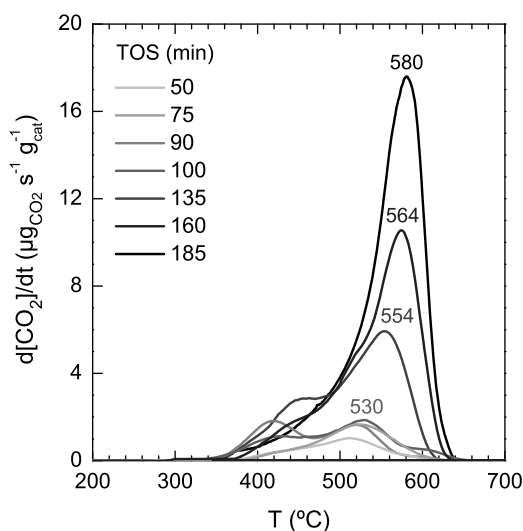**Fig. 7.** Evolution with time on stream of the TPO profiles of coke combustion.

Fig. 8. Evolution with time on stream of coke content on the catalyst.

ing one or a combination of the following features: (i) location, on the metallic sites and thus being spatially close to them, which promote both coke combustion and gasification; and/or (ii) composition, with higher content of aliphatics that creates imperfections on the stacked graphitic layers (making it more amorphous) and provoke the faster combustion of this coke [43–45,52,77,78]. This amorphous coke corresponds to the encapsulating coke observed before (Figs. 4 b, c, 5 b), which hinders the adsorption of reactants, and thus has a fundamental effect on the catalyst activity loss.

On the other hand, in line with the cited works, the combustion peak at higher temperatures (>500 °C) in Fig. 7 corresponds with the combustion of coke spatially distant from the metallic centers and/or with higher content of aromatics (higher stacking of larger graphitic layers). The larger graphitic layers have been shown in XRD diffraction pattern. This peak, at high combustion temperature, corresponds to the filamentous coke observed before (Figs. 4 d–f, 5 c–g). The formation of filamentous coke generally does not have a direct influence on catalyst deactivation, as it does not block metallic sites [44], except when its content is severe and a consid-
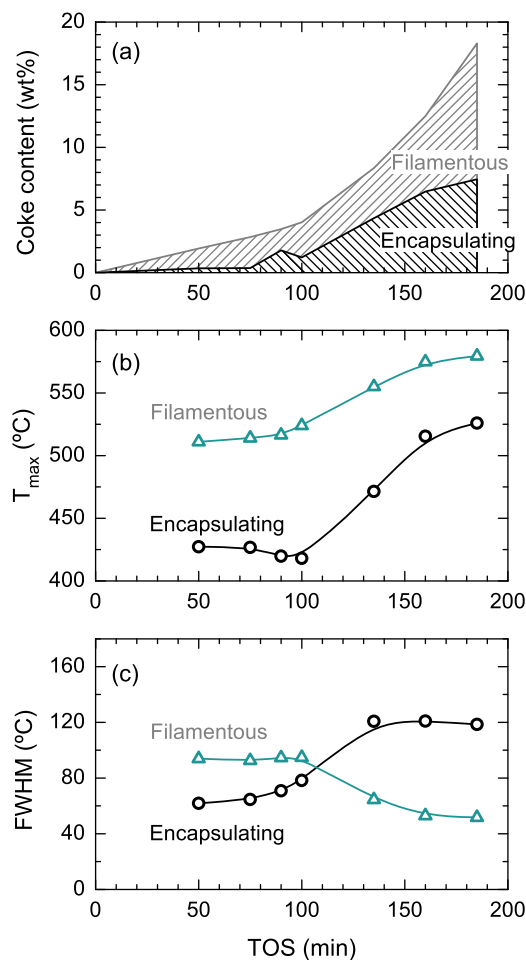
erable pore blocking takes place, thus hindering access to reactants [46].

Fig. 8 shows the evolution with the time on stream of different parameters of coke resulting from the deconvolution (in two Gaussian peaks) and integration of the TPO profiles shown in Fig. 7: Fig. 8a, coke content and fractions; Fig. 8b, temperature of the maximums (T_{max}); and Fig. 8c, peak full width at half maximum (FWHM). The evolution of coke contents (Fig. 8a) indicates that the growth of both types of coke, encapsulating and filamentous, follows two different rates: 0–100 min, with coke formation rates of 1.3 and 2.7 g_{coke} g_{cat}^{-1} min^{-1}, respectively; and 100–185 min, with the corresponding rates of 7.5 and 9.1 g_{coke} g_{cat}^{-1} min^{-1}. These values indicate that the growth rate of filamentous coke is always higher than that of the encapsulating coke, and at the same time, the step increase between the two rates is higher for the latter (6 times) compared with the former (3 times). Overall, these results point in the direction that the deactivation performance (Fig. 1, faster in the 100–185 min period) is strongly influenced by the growth of encapsulating coke, rather than that of the filamentous one, in agreement with other results of the literature [43–45,70,79–81]. Fig. 8b shows that the values of T_{max} remain constant in the first period (0–100 min) and increase significantly in the second one (100–185 min), pointing to the fact that both types of coke keep their nature in the first period and carbonize further in the second one (due to the dehydrogenation of aliphatics, the growth of graphitic layers and the stacking order of them). A similar evolution of coke and its progressive graphitization was also determined by TPO analysis by Vicente et al. [44] during the steam reforming of
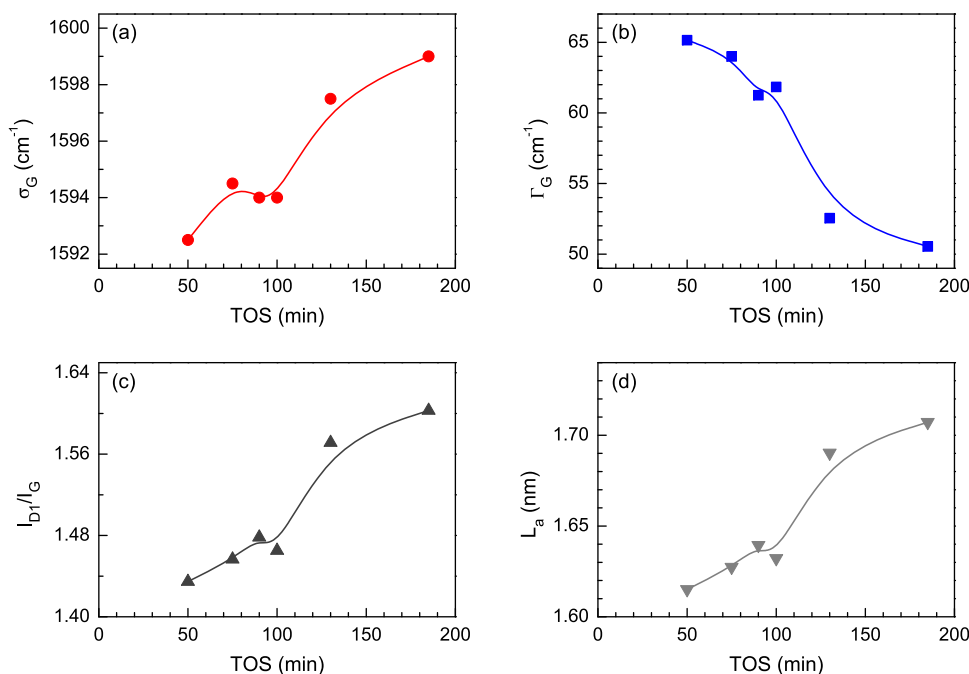
Fig. 9. Evolution with time on stream of representative Raman parameters of the coke deposited: G band position (σ_G) (a); G band width (Γ_G) (b); I_{D1}/I_G ratio (c); size of carbon domain (L_a) (d).

ethanol. Besides, Fig. 8c shows that the heterogeneity of the coke (related with the peak FWHM) is higher for the filamentous coke than that of the encapsulating one in the first period, whereas this trend is reversed in the second period. All the observations distilled from Figs. 7 and 8 imply that the formation of both types of coke, encapsulating and filamentous, coexists with that of transformation with a step change in the rates of formation and transformation at 100 min. This change may be triggered by one or a combination of the two following factors, known as inducers of a change in the coking mechanism: (i) the continuous sintering of Ni (Fig. 3), that also has a sudden change in rate at the same time (100 min), and/or (ii) the change of the reaction medium composition (Fig. 1).

3.5. Coke composition dynamics

With the aim of studying further the evolution of coke nature deposited on the catalyst, Raman spectroscopic analysis of deactivated catalysts was performed at different values of time on stream (50, 75, 90, 100, 135 and 185 min). Raman spectra were recorded in the 1000–1800 cm^{-1} wavenumber region, shown in Fig. SI-1 as Supporting information. The spectra were deconvoluted into four Lorentzian peaks (G, D1, D3 and D4), ascribed to: (i) G band (1575–1600 cm^{-1}), characteristic of graphitic layers [82–84], that is to say, stretching vibrations of sp^2 bonds in aromatic clusters [82,85,86]; (ii) D1 band (1350–1380 cm^{-1}), corresponding to the sp^2 bond vibrations close to the edges in the graphitic layers [84,87]; (iii) D3 band (1450–1510 cm^{-1}) assigned to amorphous coke in turbostratic fashion due to bond vibrations close to the edges in highly disordered graphitic layers [84,87]; (iv) D4 band (~1200 cm^{-1}), assigned to sp^2-sp^3 bond vibrations in disordered graphitic layers, with aliphatic chains [82,84,87,88].

Fig. 9 shows the evolution with time on stream of four characteristic parameters determined from the deconvolution of Raman spectra: (i) G band position (σ_G, cm^{-1}); (ii) G band FWHM (Γ_G, cm^{-1}); (iii) ratio of intensities of D1 and G bands (I_{D1}/I_G); (iv) size of carbonaceous particle or domain (L_a, nm). Together analyzed, these four parameters enable the study of the degree of order, aromatization or approximate size of carbonaceous domains [83,89,90]. The

determination of the estimated size of carbonaceous particle (L_a) was carried out attending to the values of σ_G, Γ_G and I_{D1}/I_G [83]. Based on this criterion, the expression in Eq. (7) was used, valid for values of $L_a < 2$ nm, where carbonaceous structure is closer to be amorphous rather than crystalline [83].

$$\frac{I_{DI}}{I_G} = E(\lambda)L_a^2 \tag{7}$$

where $E(\lambda)$ is a constant dependent on the excitation wavenumber (λ) employed for the analysis, using $E(\lambda = 514 \text{ nm}) \approx 0,55$ in this work [91].

The results in Fig. 9 show the following overall evolution trend with time on stream: increase in the G band position (σ_G), decrease in the G band width (Γ_G), increase in the I_{D1}/I_G area ratio and increase of the carbonaceous domain size (L_a). According to the studies in the literature [83,89,91], these results correspond to the carbonization of turbostratic and highly disordered coke (with aliphatic sp^3 bonds), into a more condensed and stacked structure (approaching to the so-called nano-crystalline carbon). During these dynamics, the stacking defects of the graphitic layers/clusters decrease at the same rate as these layers/clusters grow and the aliphatic bonds decrease. These results indicate that the deposition of coke on the catalyst (Fig. 8a), coexist with that of evolution of its composition (carbonization) towards more ordered (Fig. 9a–c) and bigger (Figs. 2 and 9 d) carbonaceous structures. Besides, two stages of coke deposition and carbonization are observed in the evolution of time on stream in Fig. 9, with an inflexion point at 100 min, coinciding with the observations obtained previously for coke and Ni.

The most representative bands of the FTIR were assigned to the following functional groups in the deposited coke [17,85,92–95]: polycondensed aromatic structures or the so called coke band, 1580 cm^{-1}; dienes and/or conjugated double bonds, 1610–1645 cm^{-1}; aliphatic −CH and −CH$_2$ bonds, 2900–2920 cm^{-1}; and aliphatic −CH$_3$ groups, 2960 cm^{-1}. The FTIR spectra were deconvoluted into these 4 Lorentzian peaks in the mentioned band positions, and shown in Fig. SI-2 as Supporting information. Fig. 10 shows the evolution of the intensities of the
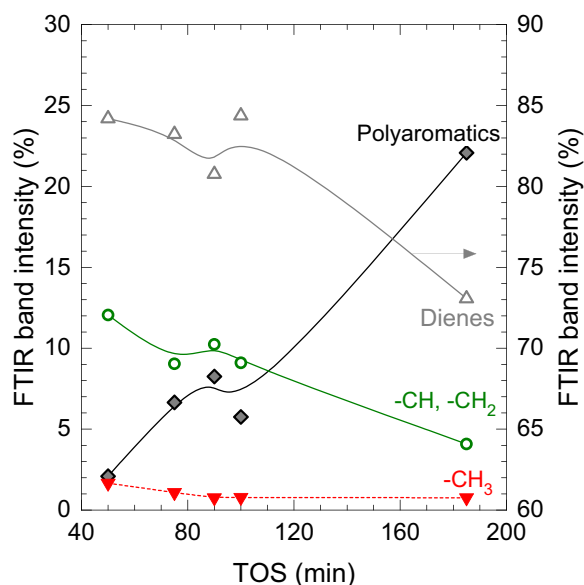
Fig. 10. Evolution with time on stream of the relative area of several representative FTIR bands corresponding to functional groups in the deposited coke.

most representative bands with time on stream. It is interesting to note that the cited band positions are approximate and little deviations took place due to the deconvolution process. The results in Fig. 10 confirm the previous discussed carbonization process of the coke, as aliphatic groups and double bounds are being transformed into more highly aromatic structures. At very short time on streams, coke is similar in nature to the reactants, constituted mainly by long chains of aliphatics with single and double bonds (C_{21+} waxes in Table 1), and then as coke build up on the catalyst it dehydrogenates (carbonize) leading to a higher fraction of polycondensed aromatic structures.

Aiming the identification of the adsorbed promoters of coke formation and growth, Fig. 11 shows the LDI-TOF MS spectra of promoters deposited on the catalyst up to 200 amu, corresponding to representative values of time on stream. The spectra show that the main fraction is lighter than that studied in the steam and oxidative reforming of acetic acid using Pt/CeO_2 o Pt/ZrO_2 catalysts [96], or in the cracking of ethanol using zeolites [97], raw bio-oil/vacuum-gas-oil [98], isobutene/butane [99] or the typical feed of a commercial FCC unit [100]. This difference indicates that in our own case, only the lighter fraction of coke (promoters) can be desorbed/ionized due to its nano- and micro-texture involving encapsulating and filamentous coke. Fig. 11 depicts an increasing heterogeneity of the adsorbed coke promoter nature with time on stream, observed by an increasing trend in the width of the mass distribution. Furthermore, this broadening of the distribution evolves towards heavier species. At lower time on stream (90 min, Fig. 11a) the spectra shows a great amount of peaks with an adjacent distance of 1 amu between them, whereas at higher times on stream (Fig. 11b, c) the number and intensity of peaks with 1 amu distance are decreased. These results indicate a decreasing trend in hydrogen content present in coke with time on stream, in line with the FTIR results in Fig. 10, where a decrease in the content of aliphatic groups is observed. Moreover, at 90 min (Fig. 11a) patterns divided by 14 amu are observed (blue arrows), corresponding to aliphatic CH_2 groups in the structure. The proportion of these patterns is decreased with time on stream, in line with the decreasing trend of aliphatics content by FTIR (Fig. 10). At the same time, an increase is observed with time on stream in the amount of patterns divided by 12 amu (red arrows), corresponding to carbon atoms from aromatic and highly unsaturated polyaromatics within the coke structure.
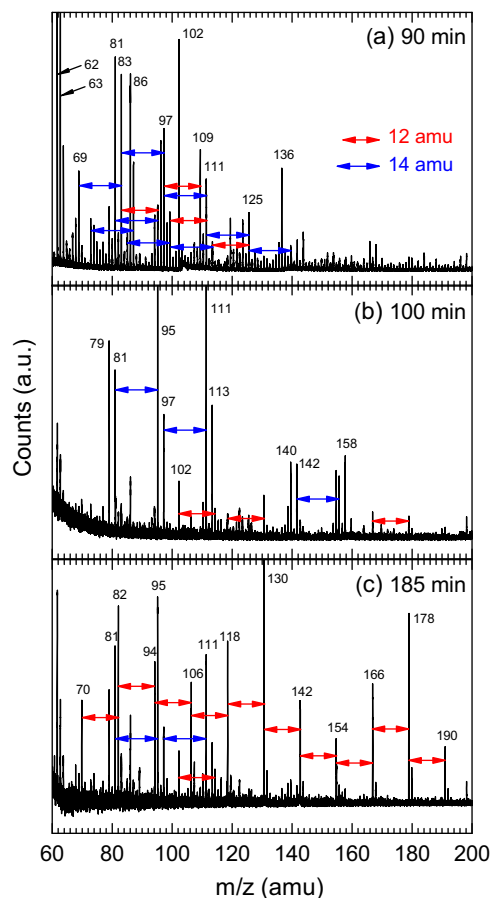

Fig. 11. LDI-TOF MS spectra of coke in the region of 60–200 amu, at 90 min (a), 100 min (b), and 185 min (c).

This trend of coke aromatization and condensing with time on stream is in line with the results of TPO (Fig. 8) and Raman and FTIR spectroscopic analysis (Fig. 9 and Fig. 10, respectively).

Based on the position of bands in the spectra of Figs. 11a–c, Fig. 12 depicts the proposed structures of adsorbed coke precursors at studied time on stream values. At lower time on stream (90 min) deposited coke possesses a more aliphatic nature, with single and double bonds. As time on stream increases, adsorbed coke precursors evolve towards a more aromatic and condensed nature, and thus increasing its molecular weight, with two or more aromatic rings attached.

The composition of the filamentous coke shown in this section indicates that this material cannot be classified as CNT. However, filamentous coke shows great potentiality of further carbonization (and graphitization), at severer temperature conditions than the one used in the reforming step of this work, in order to exploit its potential commercialization.

4. Discussion

The aforementioned results show the existence of two phenomena which contribute to catalyst deactivation during the steam reforming of HDPE pyrolysis volatiles: (i) an increase in the Ni crystal size, and; (ii) coke formation, whose content and nature evolve significantly with time on stream. It is noteworthy that the decrease of the reaction indices with time on stream has an increasing rate (Fig. 1), which may be related with both Ni sintering and coke formation-growth, with two differentiated steps (Fig. 7) with a breaking point at 100 min (ca. 5 wt% of coke on the catalyst). Addi-
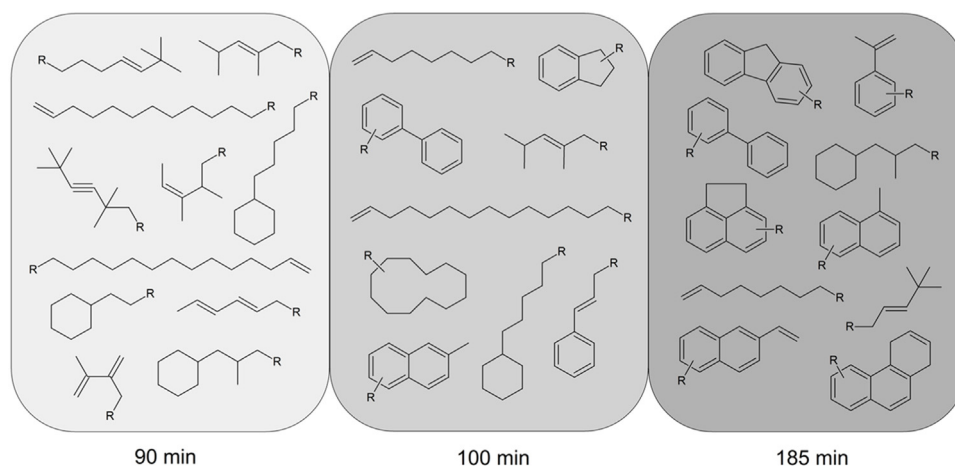
Fig. 12. Proposed chemical structure of adsorbed coke promoters based on LDI-TOF MS analysis.
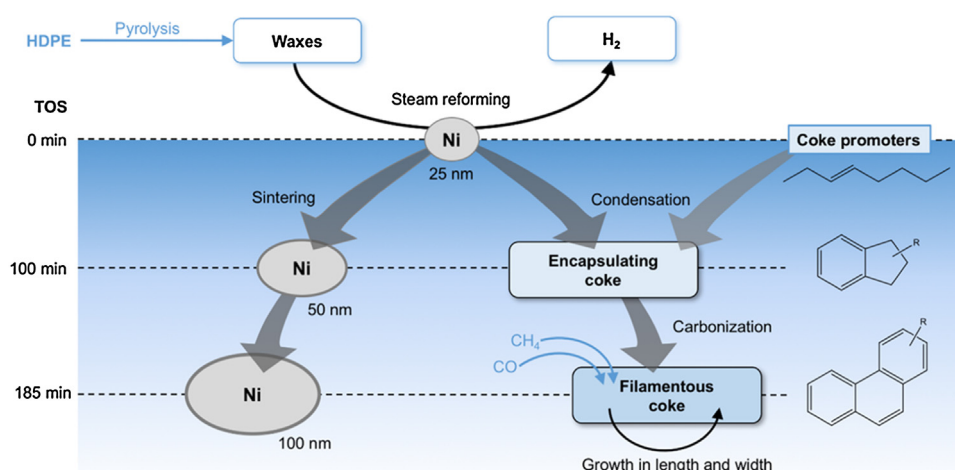

Fig. 13. Scheme of the catalyst deactivation mechanism.

tionally, it has been proved that coke is being carbonized with time on stream.

The catalytic deactivation is due to the simultaneous sintering and encapsulation (by coke) of Ni sites, whereas the formation of filamentous coke does not significantly block active sites [43–45,70,79–81]. The initial catalyst deactivation (Fig. 1) may be correlated with the deposits directly formed from the feed (waxes), or formed from the polymerization of it. The amount of these deposits increase up to a point of partially encapsulating Ni particles (Figs. 4 and 5). At 100 min on stream, the rates at which Ni sinters and coke grows (filamentous and encapsulating in particular) are increased significantly. Thus, the conversion of HDPE pyrolysis volatiles and yields of H_2, CO and CO_2 decrease more rapidly, whereas these of CH_4 and C_2–C_4 and C_{5+} increase quicker. The formation of coke coexists with its carbonization, proved by the results of TPO (Figs. 7 and 8), Raman spectroscopy (Fig. 9), FTIR spectroscopy (Fig. 10), and LDI-TOF MS (Fig. 11). This carbonization is due to the growth of graphitic layers and at the same time the higher stacking of those, in nano- and micro-textures forming multi-walled filamentous coke, as shown by SEM (Fig. 4) and TEM (Fig. 5). This multi-walled filamentous coke is responsible of the apparent increase in the surface area and porosity at 185 min (Table 2).

In the steam reforming of hydrocarbons, the main coke precursors are considered to be olefins and ethylene in particular, CH_4

and CO. That is to say, the mechanisms of coke formation can be ascribed to the polymerization of olefins, CH_4 dehydrogenation and Boudouard reaction. In the steam reforming of HDPE pyrolysis volatiles, the main adsorbed precursors of coke are hydrocarbons that evolve from napthenes and long chain olefins (reassembling the feed) towards aromatic molecules (Fig. 12). This "primordial" deposits constitute the encapsulating coke that condensate further and carbonize in order to form filamentous coke. The observed steps of coke formation and growth could not be related with the CH_4 dehydrogenation or the Boudouard reactions, respectively as the concentrations of both CH_4 and CO are relatively low. On the other hand, the steps of coke formation and growth could be linked with the sintering of Ni (Fig. 3) and the changes of composition of the adsorbed promoters of coke (Fig. 12). Thus, the overall mechanism displayed in Fig. 13 would involve a sequential process comprising the formation of encapsulating coke and subsequent transformation of that to filamentous coke (with a substantial growth in both length and diameter of the filaments), being the former one the responsible of the observed deactivation. At the same time, this mechanism is related with the sintering pathway of Ni. At 100 min there is a turning point in the rate of coke formation and carbonization, suggesting more than a plausible change of mechanism.

Ni particles sinter at a rate of approximately 20 nm h^{-1}. Several authors claim that a decrease in the Ni particle size lowers the coke

deposition and thus Ni sintering favors this deposition [45,101]. Osaki [102] highlights the fact that a lower Ni size favors coke gasification with CO_2 by inverse Boudouard reaction. In line with the observations by these authors, deactivation is more rapid in conditions in which catalyst has suffered from a severe deactivation (time on stream above 100 min). Filamentous coke is interesting from the economical perspective of the process, but according to its composition (Figs. 4–10), it requires further carbonization and graphitization in order to lead to CNTs with the proper features.

5. Conclusions

The deactivation of the Ni catalyst in the steam reforming of a sequenced HDPE pyrolysis-steam reforming process is a consequence of a series of structural and compositional changes of the catalyst: Ni sintering and the deposition of coke. The combination of analytical techniques of coke characterization (SEM and TEM, TPO, Raman, FTIR and LDI-TOF MS) has proved to be successful to analyze the evolution with time on stream of the formation and growth of coke on the catalyst. It has been determined that the coke formation mechanism has two successive stages: (1) condensation of promoters to form amorphous encapsulating coke, with relatively higher proportion of H or aliphatics; and (2) carbonization of adsorbed coke promoters to form a filamentous coke with graphitic layers that grow in size and stacking, leading to multi-walled filamentous coke. Furthermore, there may be a contribution to the formation of filamentous coke by: (i) CH_4 dehydrogenation; and (ii) Boudouard reaction. However, in the reaction conditions employed here, the most important mechanism of coke formation is the one described before.

Adsorbed coke promoters vary in nature in the due of time toward more condensed species, from olefinic (resembling the waxes fed at the beginning of the reaction) towards more condensed aromatic species. Due to this effect, the stages of coke formation accelerate with time on stream. Encapsulating coke, particularly the one formed after 100 min, is the responsible of the catalyst activity decay observed together with the sintering of Ni, which at the same time favors the carbonization of coke.

These results open an interesting work field into the process, aiming the minimization of Ni sintering and the deposition of encapsulating coke. Both objectives can be achieved decreasing the temperature but this is somehow fixed by the reforming kinetics and thermodynamics. On the other hand, a very interesting possibility is tuning the pyrolysis step in order to modify the feed composition of the second step (steam reforming). Some other initiatives aiming the adaptation of the volatiles stream submitted to reforming may be interesting, such as methane co-feeding or co-pyrolysis with biomass.

Acknowledgments

Appendix A. Supplementary data

Supplementary data associated with this article can be found, in the online version, at http://dx.doi.org/10.1016/j.apcatb.2017.02.015.

References

[1] Association of Plastic Manufacturers Europe, An Analysis of European Plastics Production, Demand and Waste Data, European Association of Plastics Recycling and Recovery Organisations, Belgium, 2015, pp. 1–32.
[2] D. Almeida, M.d.F. Marques, Polímeros 26 (2016) 44–51.
[3] U.S. Environmental Protection Agency, Common Wastes and Materials, U.S. Environmental Protection Agency, Washington D.C, 2014.
[4] W.C. Li, H.F. Tse, L. Fok, Sci. Total Environ. 566–567 (2016) 333–349.
[5] S.M. Al-Salem, P. Lettieri, J. Baeyens, Prog. Energy Combust. Sci. 36 (2010) 103–129.
[6] S.D. Anuar Sharuddin, F. Abnisa, W.M.A. Wan Daud, M.K. Aroua, Energy Convers. Manage. 115 (2016) 308–326.
[7] E. Butler, G. Devlin, K. McDonnell, Waste Biomass Valorization 2 (2011) 227–255.
[8] S.L. Wong, N. Ngadi, T.A.T. Abdullah, I.M. Inuwa, Renew. Sustain. Energy Rev. 50 (2015) 1167–1180.
[9] R. Miandad, M.A. Barakat, A.S. Aburiazaiza, M. Rehan, A.S. Nizami, Process Saf. Environ. Prot. 102 (2016) 822–838.
[10] G. Elordi, M. Olazar, G. Lopez, M. Artetxe, J. Bilbao, Ind. Eng. Chem. Res. 50 (2011) 6650–6659.
[11] G. Elordi, M. Olazar, G. Lopez, M. Artetxe, J. Bilbao, Ind. Eng. Chem. Res. 50 (2011) 6061–6070.
[12] G. Elordi, M. Olazar, M. Artetxe, P. Castaño, J. Bilbao, Appl. Catal. A: Gen. 415–416 (2012) 89–95.
[13] P.J. Donaj, W. Kaminsky, F. Buzeto, W. Yang, Waste Manage. 32 (2012) 840–846.
[14] V.K. Kaimal, P. Vijayabalan, Energ. Convers. Manage. 105 (2015) 951–956.
[15] B. Kunwar, H.N. Cheng, S.R. Chandrashekaran, B.K. Sharma, Renew. Sustain. Energy Rev. 54 (2016) 421–428.
[16] C.A. Rinaldini, E. Mattarelli, T. Savioli, G. Cantore, M. Garbero, A. Bologna, Fuel 183 (2016) 292–303.
[17] M. Arabiourrutia, G. Elordi, G. Lopez, E. Borsella, J. Bilbao, M. Olazar, J. Anal. Appl. Pyrolysis 94 (2012) 230–237.
[18] J.M. Arandes, I. Torre, P. Castaño, M. Olazar, J. Bilbao, Energy Fuels 21 (2007) 561–569.
[19] J.M. Arandes, I. Torre, M.J. Azkoiti, P. Castaño, J. Bilbao, H. de Lasa, Catal. Today 133–135 (2008) 413–419.
[20] M. Artetxe, G. Lopez, G. Elordi, M. Amutio, J. Bilbao, M. Olazar, Ind. Eng. Chem. Res. 51 (2012) 13915–13923.
[21] J. Aguado, D.P. Serrano, G. San Miguel, M.C. Castro, S. Madrid, J. Anal. Appl. Pyrolysis 79 (2007) 415–423.
[22] G. San Miguel, D.P. Serrano, J. Aguado, Ind. Eng. Chem. Res. 48 (2009) 8697–8703.
[23] M. Artetxe, G. Lopez, M. Amutio, G. Elordi, J. Bilbao, M. Olazar, Chem. Eng. J. 207–208 (2012) 27–34.
[24] M. Artetxe, G. Lopez, M. Amutio, G. Elordi, J. Bilbao, M. Olazar, Ind. Eng. Chem. Res. 52 (2013) 10637–10645.
[25] S. Czernik, R.J. French, Energy Fuels 20 (2006) 754–758.
[26] C. Wu, P.T. Williams, Energy Fuels 22 (2008) 4125–4132.
[27] C. Wu, P.T. Williams, Appl. Catal. B: Environ. 87 (2009) 152–161.
[28] C. Wu, P.T. Williams, Energy Fuels 23 (2009) 5055–5061.
[29] C. Wu, P.T. Williams, Appl. Catal. B: Environ. 90 (2009) 147–156.
[30] C. Wu, P.T. Williams, Appl. Catal. B: Environ. 96 (2010) 198–207.
[31] C. Wu, P.T. Williams, Fuel 89 (2010) 3022–3032.
[32] J.C. Acomb, C. Wu, P.T. Williams, Appl. Catal. B: Envirom. 147 (2014) 571–584.
[33] Y. Park, T. Namioka, S. Sakamoto, T.-j. Min, S.-a. Roh, K. Yoshikawa, Fuel Process. Technol. 91 (2010) 951–957.
[34] T. Namioka, A. Saito, Y. Inoue, Y. Park, T.-j. Min, S.-a. Roh, K. Yoshikawa, Appl. Energy 88 (2011) 2019–2026.
[35] A. Erkiaga, G. Lopez, I. Barbarias, M. Artetxe, M. Amutio, J. Bilbao, M. Olazar, J. Anal. Appl. Pyrolysis 116 (2015) 34–41.
[36] I. Barbarias, G. Lopez, J. Alvarez, M. Artetxe, A. Arregi, J. Bilbao, M. Olazar, Chem. Eng. J. 296 (2016) 191–198.
[37] N.V. Parizotto, K.O. Rocha, S. Damyanova, F.B. Passos, D. Zanchet, C.M.P. Marques, J.M.C. Bueno, Appl. Catal. A: Gen. 330 (2007) 12–22.
[38] K.Y. Koo, S.-h. Lee, U.H. Jung, H.-S. Roh, W.L. Yoon, Fuel Process. Technol. 119 (2014) 151–157.
[39] F. Alenazey, C.G. Cooper, C.B. Dave, S.S.E.H. Elnashaie, A.A. Susu, A.A. Adesina, Catal. Commun. 10 (2009) 406–411.
[40] N. Latorre, E. Romeo, F. Cazaña, T. Ubieto, C. Royo, J.I. Villacampa, A. Monzón, J. Phys. Chem. C 114 (2010) 4773–4782.
[41] N. Latorre, E. Romeo, J.I. Villacampa, F. Cazaña, C. Royo, A. Monzón, Catal. Today 154 (2010) 217–223.
[42] N. Latorre, F. Cazaña, V. Martínez-Hansen, C. Royo, E. Romeo, A. Monzón, Catal. Today 172 (2011) 143–151.

[43] J. Vicente, J. Ereña, C. Montero, M.J. Azkoiti, J. Bilbao, A.G. Gayubo, Int. J. Hydrogen Energy 39 (2014) 18820–18834.
[44] J. Vicente, C. Montero, J. Ereña, M.J. Azkoiti, J. Bilbao, A.G. Gayubo, Int. J. Hydrogen Energy 39 (2014) 12586–12596.
[45] C. Montero, A. Ochoa, P. Castaño, J. Bilbao, A.G. Gayubo, J. Catal. 331 (2015) 181–192.
[46] G. Słowik, M. Greluk, A. Machocki, Mater. Chem. Phys. 173 (2016) 219–237.
[47] J. Vicente, A.G. Gayubo, J. Ereña, A.T. Aguayo, M. Olazar, J. Bilbao, Appl. Catal. B: Environ. 130–131 (2013) 73–83.
[48] J. Vicente, J. Ereña, L. Oar-Arteta, M. Olazar, J. Bilbao, A.G. Gayubo, Ind. Eng. Chem. Res. 53 (2014) 3462–3471.
[49] A. Remiro, B. Valle, A.T. Aguayo, J. Bilbao, A.G. Gayubo, Energy Fuels 27 (2013) 7549–7559.
[50] J. Sehested, Catal. Today 111 (2006) 103–110.
[51] J. Sehested, J.A.P. Gelten, S. Helveg, Appl. Catal. A: Gen. 309 (2006) 237–246.
[52] A. Remiro, B. Valle, A.T. Aguayo, J. Bilbao, A.G. Gayubo, Fuel Process. Technol. 115 (2013) 222–232.
[53] B. Valle, B. Aramburu, A. Remiro, J. Bilbao, A.G. Gayubo, Appl. Catal. B: Environ. 147 (2014) 402–410.
[54] P.J. Baldock, A. Parker, I. Sladdin, J. Appl. Crystallogr. 3 (1970) 188–191.
[55] A. Utsunomiya, K. Tanaka, H. Morikawa, F. Marumo, H. Kojima, J. Solid State Chem. 75 (1988) 197–200.
[56] C. Pirlot, I. Willems, A. Fonseca, J.B. Nagy, J. Delhalle, Adv. Eng. Mater. 4 (2002) 109–114.
[57] K.M. Hardiman, C.G. Cooper, A.A. Adesina, R. Lange, Chem. Eng. Sci. 61 (2006) 2565–2573.
[58] R. Trane, S. Dahl, M.S. Skjøth-Rasmussen, A.D. Jensen, Int. J. Hydrogen Energy 37 (2012) 6447–6472.
[59] Y. Zhang, C. Wu, M.A. Nahil, P. Williams, Energy Fuels 29 (2015) 3328–3334.
[60] R.T.K. Baker, Catal. Rev. -Sci. Eng. 19 (1979) 161–209.
[61] R.T.K. Baker, Carbon Fibers Filaments and Composites, Springer, Netherlands, Dordrecht, 1990, pp. 405–439.
[62] D.L. Trimm, Catal. Today 49 (1999) 3–10.
[63] D. Chen, K.O. Christensen, E. Ochoa-Fernández, Z. Yu, B. Tøtdal, N. Latorre, A. Monzón, A. Holmen, J. Catal. 229 (2005) 82–96.
[64] A.M. Karim, Y. Su, J. Sun, C. Yang, J.J. Strohm, D.L. King, Y. Wang, Appl. Catal. B: Environ. 96 (2010) 441–448.
[65] S. Helveg, J. Sehested, J.R. Rostrup-Nielsen, Catal. Today 178 (2011) 42–46.
[66] J.L. Figueiredo, C.A. Bernardo, Carbon Fibers Filaments and Composites, Springer, Netherlands, Dordrecht, 1990, pp. 441–457.
[67] J.C. Acomb, C. Wu, P.T. Williams, Appl. Catal. B: Environ. 180 (2016) 497–510.
[68] J.C. Acomb, C. Wu, P.T. Williams, J. Anal. Appl. Pyrolysis 113 (2015) 231–238.
[69] J. Rostrup-Nielsen, D.L. Trimm, J. Catal. 48 (1977) 155–165.
[70] D.L. Trimm, Catal. Today 37 (1997) 233–238.
[71] P.H. Blanco, C. Wu, P.T. Williams, Int. J. Hydrogen Energy 39 (2014) 5723–5732.
[72] M.C. Sánchez-Sánchez, R.M. Navarro, J.L.G. Fierro, Int. J. Hydrogen Energy 32 (2007) 1462–1471.
[73] L. Zhang, W. Li, J. Liu, C. Guo, Y. Wang, J. Zhang, Fuel 88 (2009) 511–518.
[74] P. Djinović, I.G. Osojnik Črnivec, B. Erjavec, A. Pintar, Appl. Catal. B: Environ. 125 (2012) 259–270.
[75] Z. He, M. Yang, X. Wang, Z. Zhao, A. Duan, Catal. Today 194 (2012) 2–8.
[76] K.-H. Lin, C.-B. Wang, S.-H. Chien, Int. J. Hydrogen Energy 38 (2013) 3226–3232.
[77] A.G. Gayubo, J. Vicente, J. Ereña, L. Oar-Arteta, M.J. Azkoiti, M. Olazar, J. Bilbao, Appl. Catal. A: Gen. 483 (2014) 76–84.
[78] J.R. Rostrup-Nielsen, Catal. Today 37 (1997) 225–232.
[79] H. Wang, Y. Liu, L. Wang, Y.N. Qin, Chem. Eng. J. 145 (2008) 25–31.
[80] F. Wang, Y. Li, W. Cai, E. Zhan, X. Mu, W. Shen, Catal. Today 146 (2009) 31–36.
[81] R. Trane-Restrup, D.E. Resasco, A.D. Jensen, Catal. Sci. Technol. 3 (2013) 3292–3302.
[82] J. Schwan, S. Ulrich, V. Batori, H. Ehrhardt, S.R.P. Silva, J. Appl. Phys. 80 (1996) 440–447.
[83] J. Robertson, Mater. Sci. Eng. R 37 (2002) 129–281.
[84] A. Sadezky, H. Muckenhuber, H. Grothe, R. Niessner, U. Pöschl, Carbon 43 (2005) 1731–1742.
[85] P. Castaño, G. Elordi, M. Olazar, A.T. Aguayo, B. Pawelec, J. Bilbao, Appl. Catal. B: Environ. 104 (2011) 91–100.
[86] B. Valle, P. Castaño, M. Olazar, J. Bilbao, A.G. Gayubo, J. Catal. 285 (2012) 304–314.
[87] J. Sourice, A. Quinsac, Y. Leconte, O. Sublemontier, W. Porcher, C. Haon, A. Bordes, E. De Vito, A. Boulineau, S. Jouanneau Si Larbi, N. Herlin-Boime, C. Reynaud, ACS Appl. Mater. Interfaces 7 (2015) 6637–6644.
[88] P. Minutolo, M. Commodo, A. Santamaria, G. De Falco, A. D'Anna, Carbon 68 (2014) 138–148.
[89] A.C. Ferrari, D.M. Basko, Nat. Nanotechnol. 8 (2013) 235–246.
[90] C. Pardanaud, C. Martin, G. Giacometti, N. Mellet, B. Pégourié, P. Roubin, Thin Solid Films 581 (2015) 92–98.
[91] A.C. Ferrari, Solid State Commun. 143 (2007) 47–57.
[92] B. Stuart, Infrared Spectroscopy: Fundamentals and Applications, John Wiley & Sons, New York, 2004.
[93] Ë Pretsch, P. Bühlmann, M. Badertscher, Structure Determination of Organic Compounds: Tables of Spectral Data, 4th ed., Springer, Berlin, 2009.
[94] M. Ibáñez, B. Valle, J. Bilbao, A.G. Gayubo, P. Castaño, Catal. Today 195 (2012) 106–113.
[95] A. Ochoa, B. Aramburu, M. Ibáñez, B. Valle, J. Bilbao, A.G. Gayubo, P. Castaño, ChemSusChem 7 (2014) 2597–2608.
[96] B. Matas Güell, I. Babich, K.P. Nichols, J.G.E. Gardeniers, L. Lefferts, K. Seshan, Appl. Catal. B: Environ. 90 (2009) 38–44.
[97] L. Pinard, S. Hamieh, C. Canaff, F. Ferreira Madeira, I. Batonneau-Gener, S. Maury, O. Delpoux, K. Ben Tayeb, Y. Pouilloux, H. Vezin, J. Catal. 299 (2013) 284–297.
[98] A. Ibarra, A. Veloso, J. Bilbao, J.M. Arandes, P. Castaño, Appl. Catal. B: Environ. 182 (2016) 336–346.
[99] A. Feller, J.-O. Barth, A. Guzman, I. Zuazo, J.A. Lercher, J. Catal. 220 (2003) 192–206.
[100] J.O. Barth, A. Jentys, J.A. Lercher, Ind. Eng. Chem. Res. 43 (2004) 2368–2375.
[101] A. Serrano-Lotina, L. Daza, J. Power Sources 238 (2013) 81–86.
[102] T. Osaki, Catal. Lett. 145 (2015) 1931–1940.